PROCEEDINGS OF SPIE

SPIEDigitalLibrary.org/conference-proceedings-of-spie

X-ray optical simulations supporting advanced commissioning of the coherent hard x-ray beamline at NSLS-II

L. Wiegart
M. Rakitin
A. Fluerasu
O. Chubar

SPIE.

Downloaded From: https://www.spiedigitallibrary.org/conference-proceedings-of-spie on 8/29/2017 Terms of Use: https://spiedigitallibrary.spie.org/ss/TermsOfUse.aspx

X-ray optical simulations supporting advanced commissioning of the coherent hard X-ray beamline at NSLS-II

L. Wiegart*[a], M. Rakitin[a], A. Fluerasu[a], O. Chubar[a]
[a]Brookhaven National Laboratory, 740 Ring Road, Upton, NY, USA 11973

ABSTRACT

We present the application of fully- and partially-coherent synchrotron radiation wavefront propagation simulation functions, implemented in the "Synchrotron Radiation Workshop" computer code, to create a 'virtual beamline' mimicking the Coherent Hard X-ray scattering beamline at NSLS-II. The beamline simulation includes all optical beamline components, such as the insertion device, mirror with metrology data, slits, double crystal monochromator and refractive focusing elements (compound refractive lenses and kinoform lenses). A feature of this beamline is the exploitation of X-ray beam coherence, boosted by the low-emittance NSLS-II storage-ring, for techniques such as X-ray Photon Correlation Spectroscopy or Coherent Diffraction Imaging. The key performance parameters are the degree of X-ray beam coherence and photon flux, and the trade-off between them needs to guide the beamline settings for specific experimental requirements. Simulations of key performance parameters are compared to measurements obtained during beamline commissioning, and include the spectral flux of the undulator source, the degree of transverse coherence as well as focal spot sizes.

Keywords: wavefront propagation simulation, X-ray optics, partial coherence, undulator source, transverse coherence

1. INTRODUCTION

Exploiting the coherence properties in the hard X-ray regime is an emerging theme at ultra-low-emittance synchrotron storage rings. The techniques making use of the X-ray transverse coherence include Coherent Diffraction Imaging (CDI) in both Bragg and forward scattering geometries and time resolved coherent scattering such as X-ray Photon Correlation Spectroscopy[1] (XPCS) or X-ray Speckle Visibility Spectroscopy[2] (XSVS). At a synchrotron source, the transvers coherence length of the X-ray beam in the hard X-ray regime is typically smaller than the phase space used in the experiments. Simulations of beamlines and experiments in these conditions therefore require partially coherent wavefront propagation methods. The simulations presented here use both the Python and browser based[3] (Sirepo, RadiaSoft LLC) implementations of Synchrotron Radiation Workshop (SRW)[4,5] to simulate beamline performance in the partial coherence regime. A 'virtual beamline' has been implemented, mimicking the characteristics of the Coherent Hard X-ray (CHX) beamline at the National Synchrotron Light Source II (NSLS-II). The main mission of the CHX beamline is the investigation of dynamics, or electron density fluctuations, in materials on length scales ranging from micrometer to Angstroms via XPCS or XSVS. Both XPCS and XSVS are the analogs of the corresponding techniques in the optical wavelength regime. X-ray wavelength give access to much smaller length scales, absorbing samples and buried interfaces. Typical samples investigated by XPCS and XSVS range from ferroelectric domains to complex fluids, polymer nanocomposites and bio-polymer gels. The requirements of XPCS and XSVS to time-resolve the length scale dependent dynamics by time series or 'snapshots' with acquisition times shorter than those of the dynamics rearrangements, make these techniques very photon hungry, in particular for fast dynamics at small length scales and/or weakly scattering samples. Both techniques are therefore used in the regime of partial transverse coherence, adjusting the phase space of the synchrotron source used in the experiments to the best compromise between the degree of transverse coherence and photon flux. Accordingly, the CHX beamline was designed to easily accomplish this trade-off and allow for optimizing conditions for each individual experiment. Partially coherent wavefront propagation simulations in SRW were used during the design phase to predict and optimize beamline performance. The effects of a non-ideal mirror height profiles and monochromator crystal imperfections were previously assessed by partially coherent wavefront propagation simulations and compared with data obtained during early beamline commissioning[6]. Other figures of merit that were evaluated via simulations during the design phase include the flux at the sample position, the focal spot size that determines the speckle size in coherent scattering pattern and the degree of transverse coherence for different beamline configurations.

*lwiegart@bnl.gov; phone 1 631 344-8064; fax 1 631 344-8189; www.bnl.gov

Advances in Computational Methods for X-Ray Optics IV, edited by Oleg Chubar,
Kawal Sawhney, Proc. of SPIE Vol. 10388, 103880N · © 2017 SPIE
CCC code: 0277-786X/17/$18 · doi: 10.1117/12.2274403

Downloaded From: https://www.spiedigitallibrary.org/conference-proceedings-of-spie on 8/29/2017 Terms of Use: https://spiedigitallibrary.spie.org/ss/TermsOfUse.aspx

To evaluate the degree of transverse coherence, the transverse coherence lengths were either extracted from the mutual intensity at the sample position or from the simulation of a Young's double slit experiment. The objective of the measurements and simulations presented here are to benchmark the performance of the CHX beamline against partial coherent wavefront propagation simulations, taking known imperfections into account and pinpointing other potential causes for performance deficits. Performance measurements are predominantly based on permanently implemented beamline components and diagnostics and compared against simulations. The 'virtual' beamline implemented for this purpose in SRW contains all optical elements of the real CHX beamline, located at the same distance from the source or with a parameter accounting for the deviation from the nominal position (e.g. in the case of the CRL transfocator that can move along the beam direction to fine tune the focal position). The parameterization of the virtual beamline follows the setup parameters of the CHX beamline, i.e. the undulator harmonic and energy is chosen by the size of the magnetic gap, the alignment of the double crystal monochromator is determined by the crystal set and requested photon energy, etc. Energy dependent parameters in the virtual beamline are linked to either tabulated values or an online database, allowing e.g. to automatically adjust the index of refraction of optical elements with a change in photon energy.

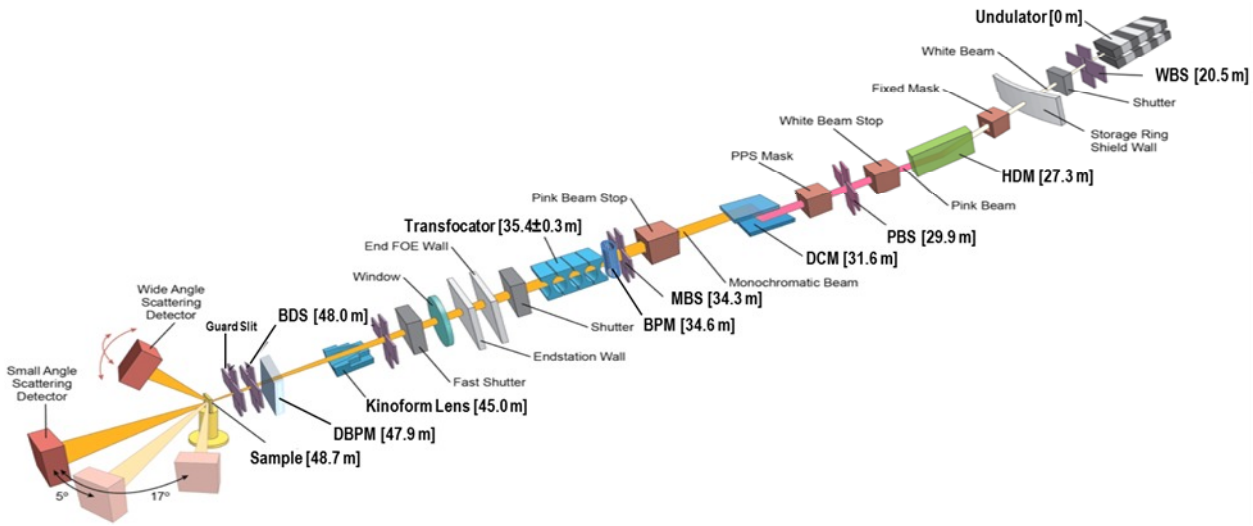

Figure 1. Sketch of the optical layout of the CHX beamline. Components used for measurements described here or included in the SRW simulations are labeled in bold, with the distance of the component from the center of the straight section indicated in square brackets.

The layout of the CHX beamline, that is also the basis for the 'virtual' beamline is shown in Figure 1. The photon source is an in-vacuum undulator (IVU) with a 20 mm magnetic period, installed in the center of the cell 11 low-β section of the storage ring (electron beam size σ and divergence σ' in horizontal and vertical direction: σ_h = 31.8 µm, σ_h' = 15.7 µrad, σ_v = 2.9 µm, σ_v' = 2.8 µrad) and followed by a set of high heatload primary slits. The first optical element is a flat, horizontally deflecting mirror (HDM), using either the bare Si substrate or a 50 nm Rh coating at a fixed incident angle of 0.18 deg. The deflected 'pink' beam can be trimmed with a set of pink beam slits (PBS) upstream of the double crystal monochromator (DCM). The DCM has two sets of crystals (Si111 and Si220, only the Si111 was used in the work presented here) in a vertical Bragg geometry with fixed gap between the crystals (pseudo-channel cut geometry). The crystals are cryo-cooled with liquid nitrogen (first crystal: side clamped, second crystal: back cooled with braid contact to the cooling loop) and the mechanics is stabilized near ambient temperature using water loops. The monochromatic beam passes a set of monochromatic beam slits (MBS), which are used to select the phase space used in the experiments. Immediately downstream of the MBS is a foil BPM that also hosts a pin-diode for absolute flux measurements and a YAG scintillation crystal and optical camera for X-ray beam visualization. Sets of 1D parabolic Beryllium refractive lenses (CRLs)[7] with radii 0.5 mm and 1.5 mm are used in a transfocator device[8] for vertical focusing in small angle X-ray scattering (SAXS) experiments. The travel range of the transfocator along the beam direction is ±300 mm. Horizontal focusing is achieved by silicon kinoform lenses[9] in kinoform unit KL1. A set of slits (PKS) just upstream of KL1 allows for selecting the lens aperture used in the experiment. For experiments in SAXS geometry, the waists of both the horizontal and vertical focus are located close to the position of the beam defining slit (BDS). After propagation to the sample position, the X-ray beam size in both horizontal and vertical direction is just below 10 µm, leading to symmetric speckle sizes in coherent scattering experiments. A diamond BPM (Sydor, 50 µm

Downloaded From: https://www.spiedigitallibrary.org/conference-proceedings-of-spie on 8/29/2017 Terms of Use: https://spiedigitallibrary.spie.org/ss/TermsOfUse.aspx

diamond thickness) just upstream of the BDS is used for stabilization of the beam position via feedback on the pitch angle of the HDM (horizontal position) and the pitch angle of the second DCM crystal (vertical position). The BDS is followed by a diagnostic module containing a pin-diode for absolute flux measurement and beam visualization via scintillation crystal and optical camera (see Methods). Parasitic scattering from the BDS can be cut before the sample position with a set of guard slits. The horizontal sample stage of the 18 axes diffractometer provides sufficient space (~0.5 m circumference), load capacity (150 kg) and positioning accuracy (< 100 nm) for a wide variety of sample environments or diagnostic tools. For SAXS experiments, sample to detector distances of up to 16 m are possible, with in-vacuum SAXS detector and beamstop.

In the scope of beamline commissioning, the CHX performance was extensively benchmarked by comparing measured radiation characteristics (spectral flux, intensity distributions at different beamline locations in its different configurations, etc.) with the corresponding calculated characteristics. The calculations were performed using "Synchrotron Radiation Workshop" (SRW), a high-accuracy synchrotron emission and wavefront propagation simulation code. In this code, a general method based on integration of the retarded potentials is used for the synchrotron radiation calculation. For the simulation of fully-coherent radiation propagation through X-ray optical elements, the code uses Fourier optics and compatible methods. Partially-coherent radiation propagation is simulated by summing up (mutual) intensities resulting from propagation of fully-coherent radiation emitted by different 'macro-electrons' distributed over phase space of the electron beam[10].

2. MEASUREMENTS AND SIMULATIONS

2.1 Spectral Flux

Similar to other project beamlines at NSLS-II, the undulator harmonics, as measured by the spectral flux through an aperture, deviated substantially from the expected characteristics. Namely, they were found to be significantly broadened and even split at higher harmonic numbers.

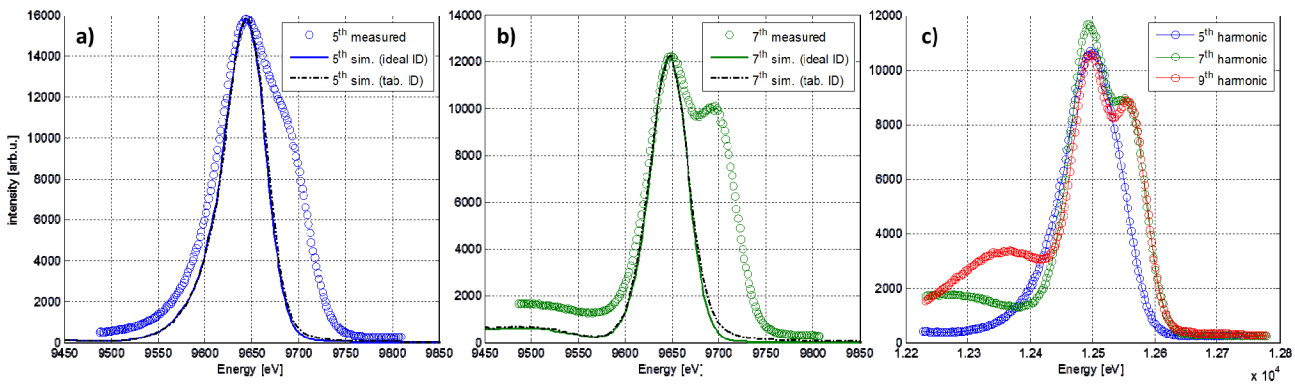

Figure 2. Initial measurements of spectral flux ('undulator harmonics'). a) measured and simulated harmonics, both for an ideal ID and using tabulated values for the magnetic field, for the 5th harmonic at 9.65keV, normalized to the maximum intensity. b) same as a) for the 7th harmonic. c) comparison of measured spectra for the 5th, 7th and 9th harmonics at 12.5keV.

Figure 2 shows the initial measurements for the 5th, 7th and 9th harmonics. The measurements used a Bragg (energy) scan of the DCM and the optical beam visualization capability of the BPM as a detector (note: the vertically deflecting DCM installed at the CHX beamline has a fixed gap between the first and the second crystal, thus the beam height is varying as a function of Bragg angle/X-ray energy. However, over the narrow energy range scanned, the beam height is virtually constant.). The position of the center of the undulator cone on the YAG was determined from the image of the undulator loops at detuned energy. The intensity in the Bragg scans was integrated in a 10x10 pixel region of interest (ROI) around this center, corresponding roughly to a 50×50 μm^2 acceptance at the position of the BPM. For these measurements all of the slits upstream of the BPM were wide open, to not affect the central part of the undulator radiation (white beam slits: 1.0×1.0 mm^2 (h×v), high heat load slits: 0.5×1.0 mm^2 (h×v), MBS: 0.4×1.0 mm^2 (h×v)). As a pre-requisite, the HDM was confirmed to be at its nominal incident angle of 0.18 deg., the DCM energy axis was calibrated using the Ti and Cu fluorescence. The roll between the second and first crystal had been corrected over the entire energy range used and the

Downloaded From: https://www.spiedigitallibrary.org/conference-proceedings-of-spie on 8/29/2017 Terms of Use: https://spiedigitallibrary.spie.org/ss/TermsOfUse.aspx

parallelism of the first and second crystal was ensured by pitch scans at the central energy of the Bragg scans or at higher energies (thereby providing higher accuracy due to the smaller Darwin width of the crystals).

The 5th and 7th harmonic at ~9.65keV (panels a) and b) in Figure 2) also show the calculated harmonics from SRW calculations. For comparison, two implementations of the IVU20 were used: 1) an idealized ID with 3m length and 20 mm magnetic period, and 2) a 'tabulated' IVU20, which uses the magnetic measurements obtained for the CHX IVU20 prior to its installation in the storage ring. The undulator harmonics were simulated in SRW as the spectral flux through an aperture at a distance from the source corresponding to the location of the BPM/MBS. In the case of the 7th harmonic, the measured data shows about twice the width of the calculated one. These findings were pointing toward a misalignment of the undulator with respect to the electron beam and/or of the undulator poles itself ('taper')[11]. Upon re-survey of the ID in the storage ring tunnel, its elevation was corrected, while the angular alignment was confirmed to be correct within survey tolerances.

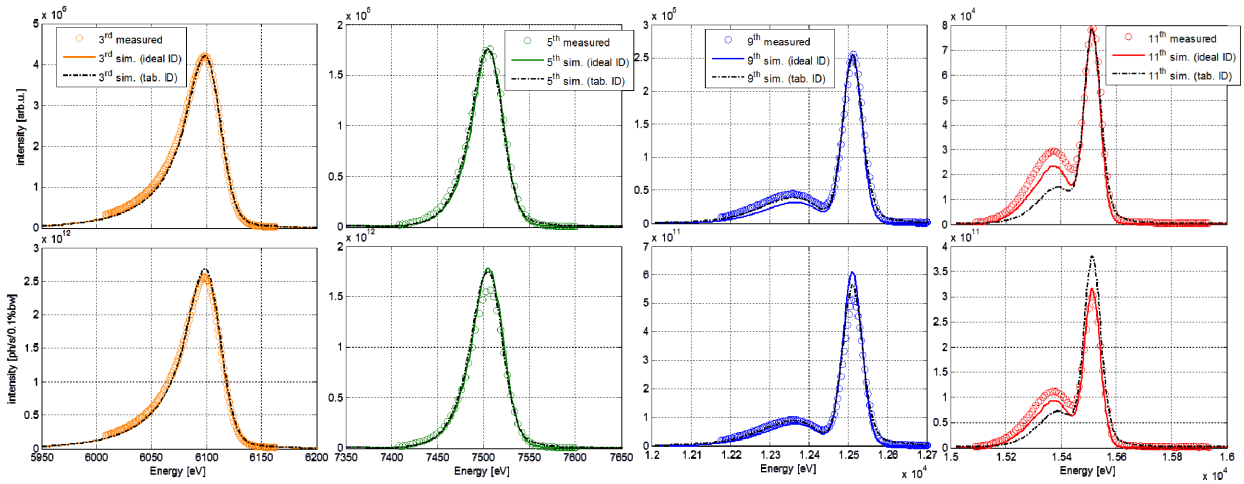

Figure 3. 3rd, 5th, 9th and 11th harmonic (left to right), spanning an X-ray energy range from 6.1 – 15.5 keV after re-survey of the ID. Top: measured and simulated harmonics scaled to have the same maximum intensity. Bottom: measurements scaled to absolute intensity using equation (2) (see Methods).

The undulator harmonics were re-measured at a storage ring current of 250 mA in top-off operation, this time using the fluorescence signal from a 600 nm Ti foil in the BPM (see Methods) and the MBS as a physical 50×50 μm^2 aperture, providing higher accuracy in the tail regions compared to the YAG measurements. In order to compare simulations and measurements on an absolute intensity scale, the photon flux (in photons per second) at the peak of the harmonic was measured using a silicon pin diode (see Methods). The obtained value was used to scale the measured and simulated harmonics to the same intensity scale. The beamline optics, namely the mirror (HDM) and double crystal monochromator (DCM) were assumed to be 'ideal' for these calculations, thus the deviations between the measured and simulated harmonics present an upper bound for possibly remaining ID magnetic field imperfections and/or misalignment with respect to the electron beam position in the straight section.

Table 1. Energy, harmonic number, corresponding ID gap, FWHM and peak intensity for the measured and simulated harmonics after first realignment of the undulator.

X-ray energy / harm. #	ID gap [mm]	$FWHM_{meas}$ [eV]	$FWHM_{ideal.ID}$ [eV]	$FWHM_{tab.ID}$ [eV]	$I_{meas.}$ [ph/s]	$I_{ideal.ID}$ [ph/s]	$I_{tab.ID}$ [ph/s]
6.1keV / 3rd	6.897	42.0	39.9	39.7	1.19×10^{11}	1.21×10^{11}	1.25×10^{11}
7.5keV / 5th	5.531	42.7	39.9	40.8	7.9×10^{10}	9.0×10^{10}	8.8×10^{10}
9.65keV / 5th	6.644	58.4	52.5	53.2	5.0×10^{10}	5.8×10^{10}	6.0×10^{10}
9.65keV / 7th	5.203	48.7	46.5	48.2	4.9×10^{10}	5.4×10^{10}	5.2×10^{10}
12.50keV / 9th	5.236	60.9	57.4	59.2	2.8×10^{10}	3.3×10^{10}	3.0×10^{10}
15.5keV / 11th	5.282	77.5	69.1	73.2	1.7×10^{10}	1.7×10^{10}	2.1×10^{10}

Downloaded From: https://www.spiedigitallibrary.org/conference-proceedings-of-spie on 8/29/2017 Terms of Use: https://spiedigitallibrary.spie.org/ss/TermsOfUse.aspx

Figure 3 shows the corresponding measurements and simulations for the 3rd (6.1 keV), 5th (7.5 keV), 9th (12.5 keV) and 11th (15.5 keV) harmonics. Significant deviations between the shape of the measured and simulated harmonics are only visible at the highest order harmonic included in this study (11th harmonic). For harmonic numbers 3 to 9, the shape, width, and absolute photon intensities for the measured and simulated spectra agree with few exceptions to within 5% (FWHM) and 10% (intensity), respectively. The corresponding values are summarized in Table 1.

A systematic study was performed during a low current machine study to further optimize the alignment between ID and electron beam. Measuring the widths of the 7th harmonic at 9.65keV (5.20mm ID gap, corresponding to the minimum allowable gap) and the 11th harmonic at the same ID gap (corresponding to a photon energy of 15.16keV), the ID elevation relative to the electron beam was systematically varied by ±150 µm. The beam defining aperture was centered on the ID cone for each measurement. The resulting FWHM of the undulator harmonics widths are shown in Figure 4 a) and b). Parabolic fits of the two datasets suggest a mean value for the elevation of about -8.5 µm, and consecutive measurements confirm the reduced width of both the 7th and 11th harmonics at this value.

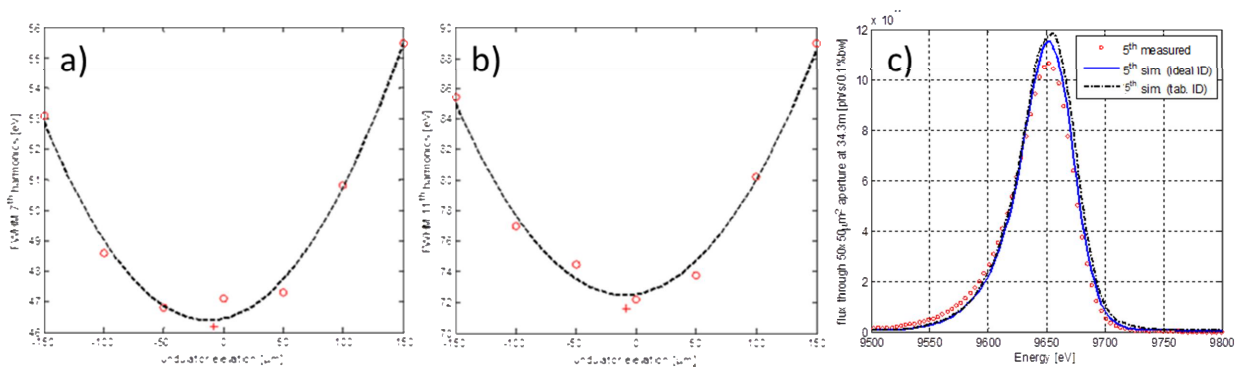

Figure 4. FWHM of the 7th (a) and 11th (b) harmonics at closed gap as a function of undulator elevation ("o" symbols). The dashed lines are parabolic fits to determine the optimum value for the elevation. (+) indicates the measurement at the optimized position. c) Measured and simulated spectra of the 5th harmonic at 9.65 keV after optimization of the undulator elevation. The simulations use the emittance value at the time of the measurements.

Figure 4 c) shows a measurement of the 5th harmonics at 9.65 keV (the currently most used X-ray energy at the beamline) after the optimization at 300 mA ring current in top-off operation. Compared to SRW simulations using the nominal storage ring parameters for emittance, the values for the FWHM are $FWHM_{meas}$ = 55.5 eV versus $FWHM_{tab.ID}$ = 53.2. SRW simulations using the actual emittance values at the time of the measurements (ε_x=0.8 nm, ε_y=30 pm, from archived machine data), show even better agreement: $FWHM_{tab.ID}$ = 54.8 eV, reducing the discrepancy between measurement and simulation to 0.7 eV. Scaled to 500 mA and the usual units (see Methods), the flux through a 50×50 μm^2 aperture at 34.3 m compares under these conditions as follows: $I_{meas.} = 1.066\times10^{12}$ ph/s/0.1%bw versus $I_{tab.ID} = 1.179 \times10^{12}$ ph/s/0.1%bw, thus experimentally observing 90.4% of the spectral flux predicted by the simulation. It is noteworthy that the simulation uses a 'perfect' mirror and monochromator and therefore lower observed flux is a combined effect of source, mirror and monochromator. As all these elements are needed simultaneously to observe spectral flux, thus experimentally assigning specific losses is not straightforward.

2.2 Focal Spot Size

The focal point in the vertical direction is located before the sample at the position of the BDS. The spot size that determines the speckle size in XPCS and XSVS experiments is the spot size at the sample. Therefore, focal spot sizes were evaluated at the sample position, using the fluorescent knife edge technique (see Methods). For the kinoform lens currently used for horizontal focusing at 9.65 keV in coherent SAXS experiments, the focal point is close to the sample position. Utilizing the flexibility that the transfocator provides in vertical focusing, the waist was also 'shifted' to the sample position and measured there. Measurements used the 5th harmonic of the undulator at 9.65keV, 300 mA top-off operations and during a run with storage ring emittance of ε_x = 0.9 nm x ε_y =23 pm. The nominal vertical focus position at the BDS is achieved at this energy by a combination of seven 1D lenses with R=0.5 mm and one lens with R=1.5 mm. To shift the waist to the sample position, the lens with R=1.5 mm was removed. The depth of vertical focus in this focal length range and energy is about 0.6 m, as defined by a 10 % increase in focal spot size as shown in Figure 5 a). The 1D Be CRLs are modeled in SRW as parabolic cylinders with the nominal 80 µm apices and without any defects. All CRLs in the virtual beamline are placed at the same distance from the source, whereas in reality and depending on the

Downloaded From: https://www.spiedigitallibrary.org/conference-proceedings-of-spie on 8/29/2017 Terms of Use: https://spiedigitallibrary.spie.org/ss/TermsOfUse.aspx

combination of lenses used, their position may vary about ± 150 mm around the nominal position of the transfocator. This approximation is justified by the long focal length (~ 13 m) in this setup. The Si kinoform lenses are currently modeled in the virtual beamline as ideal lenses, however, with physical apertures matching those of the lenses installed. In particular, the vertical aperture of the horizontally focusing kinform lens is limited by the etching depth of the kinoform structure into the silicon substrate to < 100 µm. The size of this aperture was determined by focusing the beam in the vertical plane with the transfocator at the position of the lens and vertically scanning the lens aperture across the beam.

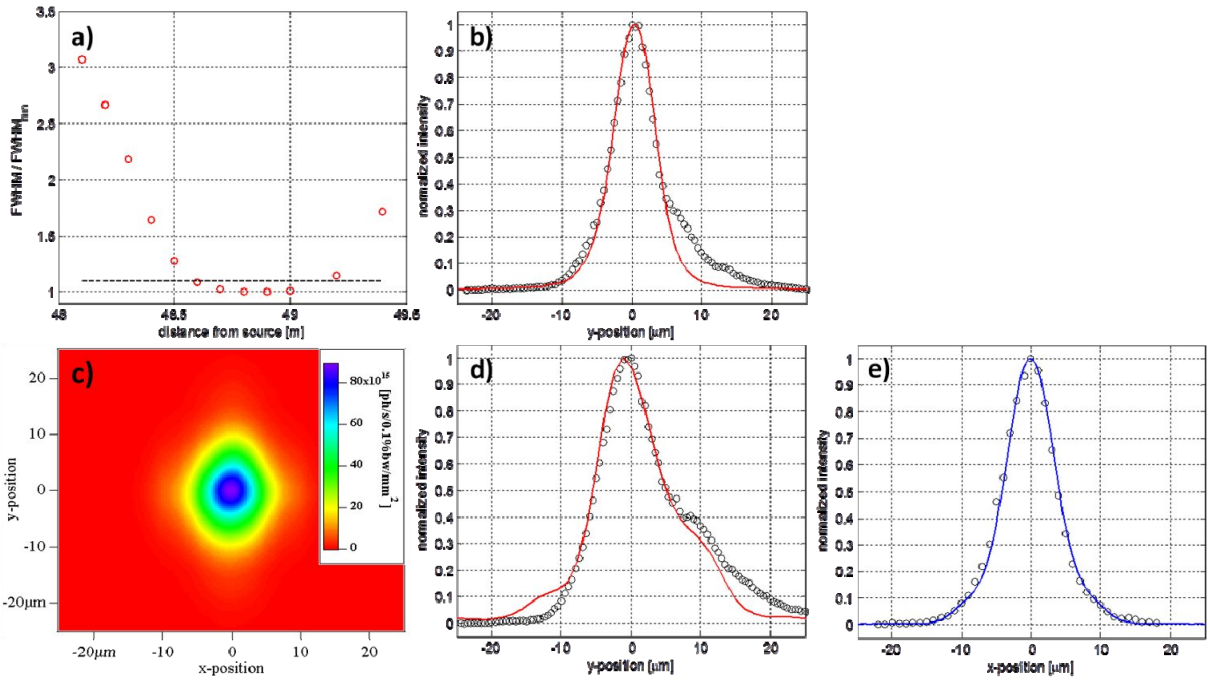

Figure 5. Horizontal and vertical focusing at 9.65 keV. a) simulation of depth of focus in the vertical direction. The dashed line indicates a 10% increase in FWHM b) vertical focus at the sample position. c) simulated 2D beam profile at the smaple position for focusing at the BDS d) vertical cut through the 2D beam profile. e) horizontal cut through the 2D beam profile.

Figure 5 b) shows the measured and simulated beam profiles for the vertical focus with the position of the waist at the sample position. Measurements were done with vertical aperture sizes for MBS (0.4 mm) and PKS (0.1 mm, matching the vertical aperture of the kinoform lens) that are typically used in coherent SAXS experiments. The 'shoulder' in the beam profile originates mostly from a known vertical misalignment of two lens stacks in the transfocator and imperfect crystal surfaces in the DCM[6]. The FWHM of the profiles were determined, without a model function, as the half intensity values of the peak intensity and are thus not affected by this shoulder. A comparison between the measured (6.94 µm) and simulated (7.10 µm) FWHM shows excellent agreement to within < 3 %. The simulated 2D beam profile for nominal focusing conditions at the sample position is shown in Figure 5 c). Simulated vertical and horizontal profiles, along with the corresponding measurements, are shown in Figure 5 d) and e). In the vertical direction, the waist is moved towards the position of the BDS by adding another CRL with R=1.5 mm. As expected, the spot size is larger than at the waist and around the 10 µm ($FWHM_{meas}$=10.4 µm, $FWHM_{sim}$=10.7 µm) design goal for the optical layout of the beamline. The horizontal spot size is slightly smaller ($FWHM_{meas}$=8.5 µm, $FWHM_{sim}$=8.3 µm). For a beam size of 0.1 mm × 0.4 mm (h×v) defined by the MBS, the measured transmission through the set of 7 × R=0.5 mm and 1 × R=1.5 mm CRLs is 82%, the value obtained by simulations (using the nominal thickness of 80 µm for the apices) is 88%. With the BDS opened to ≥ 0.05×0.05 mm^2, the measured flux for the 2D focused beam measured just downstream of the BDS is 7.7×10^{11} ph/s, compared to 1.22×10^{12} ph/s in the simulations (at Si111 bandwidth, for 500 mA storage ring current, including the transmission through the 50 µm thick diamond window in the endstation). The measured transmission for the kinoform lens is about 75%, whereas the ideal lens in the simulations has a transmission of 100%. Taking this into account, the measured flux reaches about 84% of the value in the simulations, which is consistent with the difference in transmission of the CRLs (see above) and the initial 'flux loss' attributed to source, mirror and monochromator (see Spectral Flux).

Downloaded From: https://www.spiedigitallibrary.org/conference-proceedings-of-spie on 8/29/2017 Terms of Use: https://spiedigitallibrary.spie.org/ss/TermsOfUse.aspx

2.3 Transverse Coherence

Realizing the 'simulation experiments', such as a double slit experiment, that are typically used during the beamline design phase to characterize and optimize its optical layout, is not practical during beamline commissioning. Instead, simpler means to characterize the transvers coherence length in vertical and horizontal directions are desirable, to provide a quick check of the influence of beamline and machine settings on these parameters. Slit scattering is both sensitive to the transverse coherence lengths and does not require a special diagnostic setup of the beamline. On the other hand, evaluating the measured visibility of fringes, particularly in the partially coherent regime, is not evident. A comparison with partially coherent wavefront propagation simulations, using the virtual beamline environment, provides a way of benchmarking measured versus expected beamline performance.

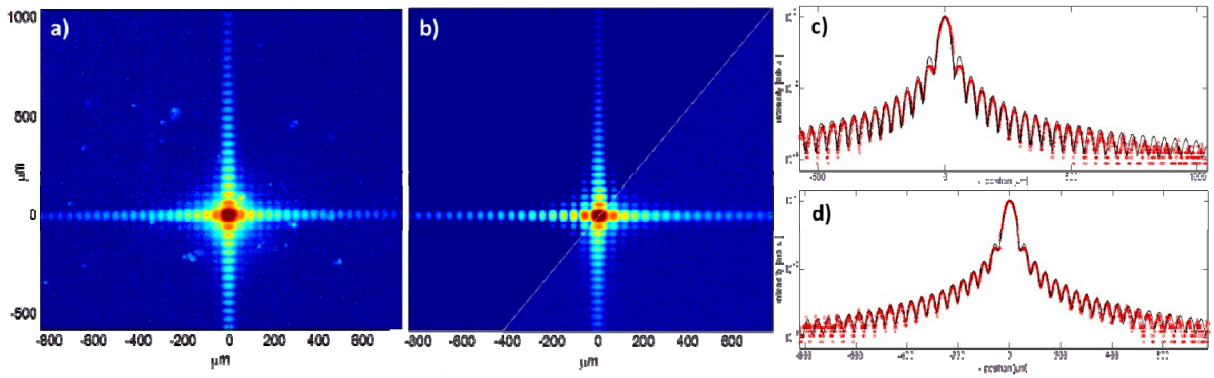

Figure 6. a) 'Pinhole' diffraction from a 19.4 × 18.5 μm^2 (h × v) PKS aperture imaged at the sample position. The irregular shaped intensity 'spots' originate in imperfections of the fluorescent screen used. b) partially coherent wavefront propagation simulation, intensity scaled to the same dynamic range as in the measurements shown in a) Above diagonal: raw simulation result; below diagonal: raw simulation data convoluted with vibrations and detector resolution; noise (originating from CCD detector) equivalent to the one observed in the measurements was added c) vertical cut through the measured diffraction pattern at x=0 (open circles) and comparison with simulation (solid line) d) horizontal cut through the measured diffraction pattern at y=0 (open circles) and comparison with simulation (solid line).

Figure 6 shows the scattering from the PKS, closed to a 19.4 × 18.5 μm^2 (h × v) 'pinhole', collected with CCD camera and fluorescence screen (see Methods) at the sample position during the early days of beamline commissioning, using an X-ray energy of 7.4 keV. At that time, the beamline did not have a feedback system and the beam stability, in particular in the vertical direction, was poor, due to vibrations of the pitch angle of the second DCM crystal. These angular vibrations were resolved up to kHz frequencies using a fast readout from the motion controller (*DeltaTau*). The cuts of the simulated scattering pattern were shifted and averaged according to the corresponding vertical deviations of the vertical beam position at the camera. The acquisition times of the camera were long compared to the timescales of the vibrations, so synchronization between camera images and vibration measurements was not required. In addition, the simulated profiles were convoluted with the known optical resolution of the camera setup (2.4 µm). The SRW simulations include imperfections of both the HDM and the DCM crystals, as described earlier[6]. The good agreement between the measured and the simulated data demonstrates the usefulness of the 'virtual beamline' approach, even under non-ideal conditions. It is noteworthy that the agreement between measured and simulated data is achieved by only taking known or independently measured parameters into account.

Figure 7 b) and c) show horizontal and vertical slit scattering from the MBS, measured with CCD camera, fluorescence screen and a pre-detector slit with 1 µm aperture size in the scanning direction. These measurements were taken after significant improvements of the beamline stability and provide high resolution beam profiles for scattering conditions spanning from almost fully coherent to partially coherent. These measurements were carried out in 300 mA top-off operations and ε_x = 0.8 nm x ε_y =30 pm at an X-ray energy of 9.65 keV, using the 5th undulator harmonic. Due to the smaller coherence length in the horizontal direction, coherent slit diffraction is limited to aperture sizes of <50 µm, giving rise to pinhole-like pattern shown in logarithmic scale in Figure 7 c). An excellent agreement in the visibility of diffraction fringes is observed over at least two orders of magnitude in intensity. Contrary, in the vertical direction the larger coherence length gives rise to diffraction fringes at much larger apertures (>400 µm, not shown). The diffraction profiles change from pin-hole like scattering (≤50 µm apertures) to modulated 'box-profiles', with intermediate profile

Downloaded From: https://www.spiedigitallibrary.org/conference-proceedings-of-spie on 8/29/2017 Terms of Use: https://spiedigitallibrary.spie.org/ss/TermsOfUse.aspx

shapes around 100 µm aperture size at this energy (see Figure 7 b). Contrary to the pinhole-like scattering the diffraction fringes at larger apertures are highly asymmetric and very sensitive to aperture size and coherence conditions (see Figure 7 a).

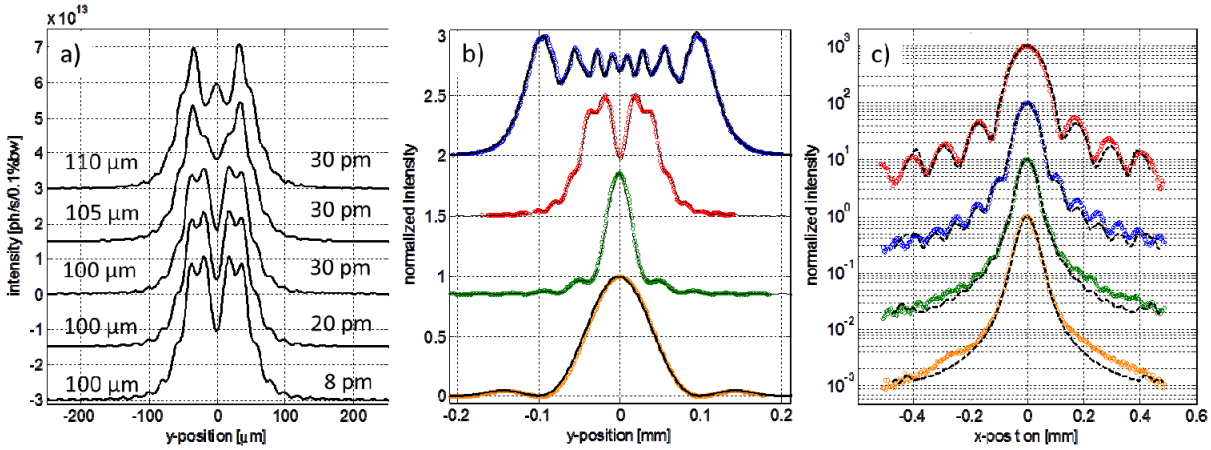

Figure 7. a) Sensitivity of slit diffraction to aperture size (values to the left of the diffraction profiles) and storage ring vertical emittance (values to the right of the diffraction profiles), demonstrated with partially coherent wavefront simulations for the vertical MBS. b) diffraction from vertical apertures of the MBS, measured at the sample position, and corresponding simulations; vertical aperture sizes: 0.2 mm, 0.1 mm, 0.05 mm, 0.02 mm (top to bottom). c) diffraction from horizontal apertures of the MBS, measured at the sample position, and corresponding simulations; horizontal aperture sizes: 0.0155 mm, 0.0255 mm, 0.0355 mm, 0.0555 mm (top to bottom).

All the blades of all slits used to create slit diffraction pattern have knife edge blades, with angles of about 2 deg. These blades were simulated as ideal apertures in SRW, showing in general good agreement. It is noteworthy that index of refraction maps, such as the height profiles of HDM and DCM[6] or of 'virtual samples'[12], provide a route to implement imperfect slit blades, where needed. Figure 8 shows an example for an aperture (in this case the BDS) defined by perfect and imperfect knife edge blades respectively. The 20×20 µm^2 aperture is defined by tungsten knife edge blades (2 deg. knife edge angle, 0.5mm thickness), which have a roughness of 85 nm in the imperfect case. Simulations were carried out at 7.4 keV.

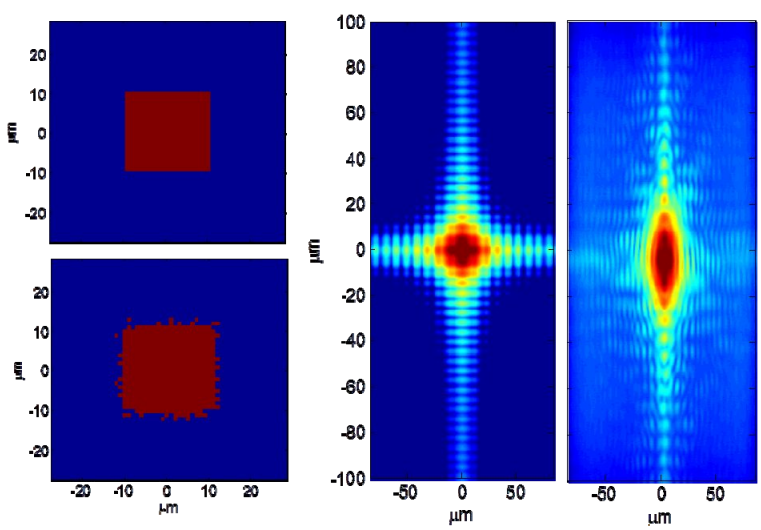

Figure 8. Comparison of perfect (left, top) and imperfect (left, bottom) aperture (20 × 20 µm^2), defined by knife edge blades. While the perfect aperture produces well defined fringes (middle), the imperfections greatly distort the fringes and reduce their visibility. Simulations use the aperture at the position of the BDS and image its diffraction pattern at the sample position.

Downloaded From: https://www.spiedigitallibrary.org/conference-proceedings-of-spie on 8/29/2017 Terms of Use: https://spiedigitallibrary.spie.org/ss/TermsOfUse.aspx

3. CONCLUSIONS

The comparison of the measured and simulated performance parameters of the CHX beamline, including spectral flux, the profile of the focused beam at and off waist, as well as transverse beam coherence show very good agreement. With the exception of the kinoform lens that is used for horizontal focusing in coherent SAXS experiments, source and optics achieve about 84 % of the spectral flux predicted by the simulations. Improving the performance of the kinoform lens, while also implementing a more realistic model in the simulations, is planned for the future. Slit scattering has been used to demonstrate sensitivity to the vertical emittance of the source and the visibility of the observed fringes matches the ones in the simulations, where only the emittance parameter was adjusted.

Overall, the virtual beamline, based on partially coherent wavefront propagation in SRW, mimics the performance of the CHX beamline correctly, not only qualitatively, but also quantitatively. This opens the route for a range of applications:

- Pinpoint and quantify problems of the real beamline, such as underperforming optics, from discrepancies between simulated and measured data.
- Use the virtual beamline to extract parameters that are difficult to measure with the real beamline, such as mutual intensity or transverse coherence length from a double slit experiment.
- Forward simulation of experimental data, using a complex index of refraction map as a 'virtual' sample. This approach provides a means to further benchmark the beamline performance under conditions relevant to coherent scattering experiments. It also enables realistic feasibility studies based on simulations for coherent scattering experiments. In the future, such simulations might be applied to solving inverse problems, i.e. extracting information about the sample from partially coherent scattering pattern.

4. METHODS

4.1 Measurements with fluorescent screen and CCD camera

The measurements based on integrating intensity over a region of interest (ROI) on a camera employed a fluorescent crystal that converts part of the incident X-rays to the visible light. The visible light is reflected at 90 deg. by a first surface mirror and imaged with a CCD camera (Prosilica GT2450B, Allied Vision). At the position of the foil BPM, a 50 mm focal length optic (Tamron 23FM50SP) is used in combination with a YAG crystal (Yttrium Aluminum Garnet), resulting in a spatial resolution of about 5µm per pixel. The imaging system at the sample position consisted of a CdWO4 fluorescent crystal and PreciseEye optics (Navitar), exhibiting an optical resolution of 2.4 µm at nominal pixel size of 0.79 µm. Image processing used the Area Detector application.

4.2 Fluorescence measurements

Bragg scans using the fluorescence signal of the BPM as the detection mode employed either a 600 nm thick Titanium foil or a 1µm thick Copper foil. The foils were selected such that their respective absorption edges were far from the energy of the harmonics and under this condition the fluorescence signal was assumed to be independent of X-ray energy over the small energy range scanned. The fluorescence signal from the foils was detected by four silicon pin diodes (Hamamatsu, S3590-09) in backscattering geometry and their current was digitalized by a four channel Picoammeter (AH401D, CAENels). The measured signal was the sum of the current from all four diodes.

4.3 Beam profile measurements with fluorescent knife edge

For a precise measurement of the focused beam profiles, the fluorescence from a 'knife edge' in combination with an energy sensitive detector was used. A thin wall, etched to about 100 µm depth into a silicon chip and topped with a thin (~50 nm) Cr layer served as a 'knife edge'. The Cr layer was scanned across the beam profile, using precision stages encoded to better than 10 nm resolution, and the X-ray signal was detected at 90 deg. scattering angle with an energy sensitive detector (Vortex SDD, Hitachi). In combination with a multi-channel analyzer (xpress3 mini, Quantum Detectors), the Cr fluorescence signal can be separated from the elastically scattered photons, so that effectively the thin Cr layer becomes the probe for the beam profile measurement.

4.4 Beam profile measurements with slit

The beam profile measurements with a fluorescent knife edge (see above) are limited by the etching depth to a scan range ≤100 µm. High resolution measurements of coherent slit diffraction require a much larger scan range and were

Downloaded From: https://www.spiedigitallibrary.org/conference-proceedings-of-spie on 8/29/2017 Terms of Use: https://spiedigitallibrary.spie.org/ss/TermsOfUse.aspx

thus carried out using a slit, set to 1 μm aperture in the scanning direction, in combination with fluorescent crystal and CCD camera. To avoid artifacts from locally varying pixel or fluorescent crystal response, the sample stages were used to move the whole setup, consisting of slit, fluorescent screen, optics and camera, during a scan. The average intensity from a scan without X-rays was subtracted to take into account the noise of the CCD camera. Measurements of coherent slit diffraction were normalized by the corresponding white field measurements, eliminating artificial features that do not stem from the slit diffraction.

4.5 Absolute X-ray intensity measurements

The absolute numbers for the measured X-ray flux were obtained with a silicon PIN diode (Hamamatsu, S3590-09) as a detector. The active area of the diode (10×10 mm^2) is significantly larger than the beam size at the location of the BPM and thus intersects the entire beam passed through the MBS. The current from the diode was amplified and converted to a voltage signal by means of a low noise variable gain current amplifier (FEMTO, DLPCA-200). The current in the PIN diode is related to the X-ray flux by[13]:

$$I = \psi e E[1 - \exp(-A_{pe} t_{Si} \rho_{Si})] / \varepsilon \tag{1}$$

where I is the measured electrical current, ψ is the X-ray flux (in photons/second), e=1.6022x10^{-19} C, E is the X-ray energy, A_{pe} is the photo electric absorption coefficient for silicon, t_{Si} = 300 μm is the thickness of the Silicon in the diode used, ρ_{Si} = 2.329 g/cm^3 is the density of Silicon and ε =3.66 eV is the energy needed to create an electron-hole pair in silicon. The energy dependent values for the photo electric absorption coefficient were calculated using the web based database XCOM[14] (NIST).

4.6 Intensity calculations

The intensity in SRW simulations has the usual units of photons/second/0.1% energy bandwidth. In order to convert it to the unit of photons/second used in the absolute intensity measurements, one needs to take into account the energy bandwidth and reflectivity of the monochromator, the reflectivity of the mirror (if not included in the simulation) and the storage ring current. The CHX beamline is windowless all the way into the endstation, thus e.g. for the spectral flux measurements there are no absorbing elements such as windows or filters to be taken into account. The relation between the measured and simulated photon flux can then be expressed as[15]:

$$N(E)_{meas.} = N(E)_{sim.} \frac{(\Delta E/E)_{\text{intr.}}}{(\Delta E/E)_{\text{sim.}}} p_0 R_{HDM} \frac{I_{meas.}}{I_{sim.}} \tag{2}$$

where $N(E)_{meas}$ is the energy-dependent number of photons measured after the monochromator and through the aperture set by the MBS. $N(E)_{sim}$ is the energy-dependent number of photons obtained by the simulation with the energy bandwidth $(\Delta E/E)_{sim.}$. $(\Delta E/E)_{intr.}$ denotes the intrinsic energy resolution of the double crystal monochromator and can be expressed in terms of the Darwin width ω_D of the reflection and the Bragg angle θ_B as $(\Delta E/E)_{intr.} = \omega_D \times cot\theta_B$. p_0 is the peak value of the double-crystal diffraction profile (i.e., the peak of the product of the crystal diffraction profile multiplied by itself). R_{HDM} is the reflectivity of the HDM, depending both on the energy and the reflective surface. Below 10keV the bare Si substrate is used, whereas for higher energies a stripe with a Rh coating of nominally 50 nm thickness is available. The last term $I_{meas.}/I_{sim.}$ scales the storage ring current, that might differ between the simulation and the measurement.

Table 2. Energy dependent values for the reflectivity of the HDM (elements in brackets indicate whether the bare Si substrate or the Rh coated stripe was used), the peak value of the double crystal diffraction profile, the Bragg angle and the Darwin width.

E (eV)	6100	7500	9650	12500	15500
R_{HDM}	0.943 (Si)	0.942 (Si)	0.881 (Si)	0.946 (Rh)	0.944 (Rh)
p_0	0.684	0.726	0.765	0.793	0.807
θ_B [deg.]	18.923	15.293	11.829	9.106	7.332
ω_D [rad]	4.95×10^{-5}	3.96×10^{-5}	3.03×10^{-5}	2.29×10^{-5}	1.85×10^{-5}

The energy dependent values for R_{HDM} were calculated using the online tools of CXRO[16], for a single thick Si mirror and a 50 nm thick Rh coating on top of a Si substrate at 0.18 deg. incident angle. All material densities were assumed to have the bulk values and all interfacial roughness values were set to 0.3 nm. The Bragg angles for a cryo-cooled (80 K) Si111

Downloaded From: https://www.spiedigitallibrary.org/conference-proceedings-of-spie on 8/29/2017 Terms of Use: https://spiedigitallibrary.spie.org/ss/TermsOfUse.aspx

crystal are taken from XOP[17]. The peak of the double crystal diffraction profile p_0 was taken from the self-convolution of the diffraction curve calculated with XOP's XINPRO tool for a perfect, flat Si111 crystal at a temperature of 80 K. The Darwin width ω_D was determined from the same diffraction profile. The energy dependent values for R_{HDM}, p_0, θ_B and ω_D used for this report are summarized in Table 2.

ACKNOWLEDGEMENT

This research used beamline 11ID (CHX) of the National Synchrotron Light Source II, a U.S. Department of Energy (DOE) Office of Science User Facility operated for the DOE Office of Science by Brookhaven National Laboratory under Contract No. DE-SC0012704. The work was partially supported by DOE SBIR grant DE-SC0011237.

REFERENCES

[1] Sphyrko, O.G., "X-ray photon correlation spectroscopy", Journal of Synchrotron Radiation 21, 1057–1064 (2014).

[2] Li, L., Kwasniewski, P., Orsi, D, Wiegart, L. Cristofolini, L., Caronna, C, Fluerasu, A., "Photon statistics and speckle visibility spectroscopy with partially coherent X-rays," Journal of Synchrotron Radiation 21, 1288-1295 (2014).

[3] RadiaSoft LLC, (8 August 2017) https://beta.sirepo.com/light#/home.

[4] Chubar, O., Elleaume, P., Proc. EPAC-98, (1998).

[5] Chubar, O.,Elleaume, P., Kuznetsov, S., Snigirev, A., "Physical Optics Computer Code Optimized for Synchrotron Radiation", Proc. *SPIE*, (2002).

[6] Wiegart, L., Fluerasu, A., Bruhwiler, D., Chubar, O., "Partially Coherent Wavefront Propagation Simulations: Mirror and Monochromator Crystal Quality Assessment", AIP Conference Proceedings, 1741, 040013 (2016).

[7] Lengeler, B., Schroer, C., Richwin, M., Tummler, J.,Drakopoulos, M., Snigirev, A., Snigireva, I., "A microscope for hard x rays based on parabolic compound refractive lenses", Appl. Phys. Let., 74(26), 3924-3926 (1999).

[8] Snigirev, A., Snigireva, I., Vaughan, G., Wright, J., Rossat, M., Bytchkov, A., Curfs, C., "High energy X-ray Transfocator based on Al parabolic refractive lenses for focusing and collimation", Journal of Physics Conference Series 186, 012073 (2009).

[9] Evans-Lutterodt, K., Ablett, J., Stein, A., Kao, C., Tennant, D., Klemens, F., Taylor, A., Jacobsen, C., Gammel, P., Huggins, H., Ustin, S., Bogart, G., Ocola, L., "Single-element elliptical hard x-ray micro-optics," Optics Express. 11(8), 919-926 (2004).

[10] Chubar, O., Berman, L., Chu, Y.S., Fluerasu, A., Hulbert, S., Idir, M., Kaznatcheev, K., Shapiro, D., Shen, Q., Baltser, J, "Development of partially-coherent wavefront propagation simulation methods for 3rd and 4th generation synchrotron radiation sources", Proc. of *SPIE* (2011).

[11] Chubar, O., Chu, Y.S., Huang, X., Kalbfleisch, S., Yan, H., Shaftan, T., Wang, G., Cai, Y., Suvorov, A., Fluerasu, A., Wiegart, L., Chen-Wiegart, Y., Thieme, J., Williams, G., Idir, M., Tanabe, T., Zschack, P., Shen, Q., "Initial Performances of First Undulator-Based Hard X-Ray Beamlines of NSLS-II Compared to Simulations", AIP Conference Proceedings, 1741, 040002 (2016).

[12] Chubar, O., Fluerasu, A., Berman, L., Kaznatcheev, K., Wiegart, L., "Wavefront propagation simulations for beamlines and experiments with "Synchrotron Radiation Workshop", Journal of Physics Conference Series 425, 162001 (2013).

[13] Owen, R., et al., J. Synchrotron Radiation 16, 143-151 (2009).

Downloaded From: https://www.spiedigitallibrary.org/conference-proceedings-of-spie on 8/29/2017 Terms of Use: https://spiedigitallibrary.spie.org/ss/TermsOfUse.aspx

[14] XCOM (8 August 2017) https://www.nist.gov/pml/xcom-photon-cross-sections-database.

[15] del Rio, M., Mathon, O., "A simple formula to calculate the x-ray flux after a double-crystal monochromator," in Proc.of SPIE (2004).

[16] Henke, B., Gulikson, E., Davis, J., "X-ray interactions: photoabsorption, scattering, transmission, and reflection at E=50-30000 eV, Z=1-92," Atomic Data and Nuclear Data Tables, 54(2), 181-342 (1993).

[17] del Rio, M., Dejus, R., "XOP 1.2 - A new version of the x-ray optics software toolkit," in *American Institute of Physics, Conference Proceedings*, (2004).

Downloaded From: https://www.spiedigitallibrary.org/conference-proceedings-of-spie on 8/29/2017 Terms of Use: https://spiedigitallibrary.spie.org/ss/TermsOfUse.aspx